Title

The accuracy of helium ion CT based particle therapy range prediction: an experimental study comparing different particle and x-ray CT modalities

Journal

Physics in Medicine and Biology, 66(23)

ISSN

0031-9155

Authors

Volz, L
Collins-Fekete, C-A
Bär, E
et al.

Publication Date

2021-12-07

DOI

10.1088/1361-6560/ac33ec

Peer reviewed

HHS Public Access

Author manuscript

Phys Med Biol. Author manuscript; available in PMC 2022 November 29.

Published in final edited form as:

Phys Med Biol. ; 66(23): . doi:10.1088/1361-6560/ac33ec.

The accuracy of helium ion CT based particle therapy range prediction: An experimental study comparing different particle and X-ray CT modalities

L. Volz[1,2,*], **C.-A. Collins-Fekete**[4], **E. Bär**[4,5], **S. Brons**[6], **C. Graeff**[3], **R. P. Johnson**[7], **A. Runz**[8], **C. Sarosiek**[9], **R. W. Schulte**[10], **J. Seco**[1,2]

[1] Department of Biomedical Physics in Radiation Oncology, Deutsches Krebsforschungszentrum (DKFZ), Heidelberg, GER

[2] Department of Physics and Astronomy, Heidelberg University, Heidelberg, GER

[3] Biophysics, GSI Helmholtz Center for Heavy Ion Research GmbH, Darmstadt, GER

[4] Department of Medical Physics and Biomedical Engineering, University College London, London, UK

[5] Department of Radiotherapy Physics, University College London Hospitals NHS Foundation Trust, London, UK

[6] Heidelberg Ion-Beam Therapy Center, Universitäts Klinikum Heidelberg, Heidelberg, GER

[7] Department of Physics, University of California at Santa Cruz, Santa Cruz, USA

[8] Department of Medical Physics in Radiation Therapy, Deutsches Krebsforschungszentrum (DKFZ), Heidelberg, GER

[9] Department of Physics, Northern Illinois University, DeKalb, USA

[10] Department of Basic Sciences, Division of Biomedical Engineering Sciences, Loma Linda University, Loma Linda, USA

Abstract

This work provides a quantitative assessment of helium ion CT (HeCT) for particle therapy treatment planning. For the first time, HeCT based range prediction accuracy in a heterogeneous tissue phantom is presented and compared to single-energy X-ray CT (SECT), dual-energy X-ray CT (DECT) and proton CT (pCT).

HeCT and pCT scans were acquired using the US pCT collaboration prototype particle CT scanner at the Heidelberg Ion-Beam Therapy Center (HIT). SECT and DECT scans were done with a Siemens Somatom Definition Flash and converted to RSP. A Catphan CTP404 module was used to study the RSP accuracy of HeCT. A custom phantom of 20cm diameter containing several tissue equivalent plastic cubes was used to assess the spatial resolution of HeCT and compare it to DECT. A clinically realistic heterogeneous tissue phantom was constructed using cranial slices

l.volz@gsi.de .

*Currently at Biophysics, GSI Helmholtz Center for Heavy Ion Research GmbH, Darmstadt GER

from a pig head placed inside a cylindrical phantom (ø150mm). A proton beam (84.67mm range) depth-dose measurement was acquired using a stack of GafchromicTM EBT-XD films in a central dosimetry insert in the phantom. CT scans of the phantom were acquired with each modality, and proton depth-dose estimates were simulated based on the reconstructions.

The RSP accuracy of HeCT for the plastic phantom was found to be 0.3±0.1%. The spatial resolution for HeCT of the cube phantom was 5.9±0.4lp/cm for central, and 7.6±0.8lp/cm for peripheral cubes, comparable to DECT spatial resolution (7.7±0.3lp/cm and 7.4±0.2lp/cm, respectively). For the pig head, HeCT, SECT, DECT and pCT predicted range accuracy was 0.25%, −1.40%, −0.45% and 0.39%, respectively.

In this study, HeCT acquired with a prototype system showed potential for particle therapy treatment planning, offering RSP accuracy, spatial resolution, and range prediction accuracy comparable to that achieved with a commercial DECT scanner. Still, technical improvements of HeCT are needed to enable clinical implementation.

Keywords

Particle CT; helium ions; Dual-Energy CT; tissue sample; range

1. Introduction

In analytical particle therapy treatment planning, highly accurate voxelized information on the patient tissue relative stopping power (RSP) is crucial to accurately predict the Bragg peak position in the patient[1]. The current clinical procedure is to derive the patient RSP map from a single-energy X-ray CT (SECT) by an empirical or stoichiometric calibration [2]. This procedure introduces conversion uncertainties in the predicted RSP due to the non-bijective relationship between the RSP and the photon absorption coefficient measured by SECT [3, 4, 1, 5]. Moreover, no standard calibration protocol among proton therapy centers exists, leading to varying center specific range uncertainty [6]. For higher quality particle therapy, improved RSP acquisition methods are therefore required.

Two promising modalities have emerged in recent years to provide a more accurate RSP map for the clinical practice of particle therapy: dual-energy X-ray CT (DECT) and proton CT. DECT utilizes two scans of the patient acquired with different photon energy spectra, giving partially complementary information. This provides for improved RSP prediction, with several algorithms reported in the literature [7, 8, 9, 10]. Recent simulation studies and experimental campaigns have shown DECT based RSP prediction to achieve better than 1% mean absolute percentage error (MAPE) [11, 12, 13, 14].

Proton CT (pCT), using the same particles for treatment and imaging, on the other hand, has been proposed as a more direct method for RSP estimation. Measuring the integral energy loss of protons after traversing the patient enables the computation of the patient's water equivalent thickness (WET), which is the line integral over the RSP. Hence, reconstruction of the voxelized RSP map is possible through pCT[15]. The expected improved accuracy of pCT over SECT-based RSP prediction, due to the direct nature of the measurement, was confirmed in recent experimental studies using plastic samples [16, 17]. Nevertheless,

plastic samples provide only a limited basis for comparison due to their poor representation of human tissues [18] and the homogeneity of the samples. deJongh *et al.* [19] conducted a relative comparison between pCT and SECT based RSP reconstruction for fresh post-mortem heterogeneous porcine tissue samples. They report acceptable agreement between the two modalities for soft tissue and larger discrepancies in bones.

In 2016, we started an experimental campaign to investigate particle CT with protons (pCT) and helium ions (HeCT) in comparison with SECT and DECT at the Heidelberg Ion Therapy Center (HIT). While most studies so far focused on pCT due to the more widespread availability of proton therapy compared to heavy ion therapy, HeCT has received increasing interest recently, as the number of combined proton and ion treatment centers is increasing worldwide. This interest in HeCT is founded in the factor-two reduced scattering and straggling of helium ions compared to protons, as well as their lower fragmentation and dose-per-primary compared to heavier ions [20, 21]. In a recent publication by Bär *et al.* [22], we have presented a comparison of the RSP accuracy of SECT, DECT, pCT and HeCT in 16 fresh post-mortem homogeneous tissue samples. Our results indicated comparable RSP accuracy between DECT and HeCT at MAPE of 0.61% and 0.68%, respectively, compared to RSP reference measurements acquired with a carbon ion beam.

To date, only few experimental studies on helium ion imaging are available, most focusing on helium radiography [23, 20, 24, 25], and works on experimental HeCT [26, 27, 22] have investigated separately the RSP accuracy, noise and spatial resolution of the reconstructed scans. While good RSP accuracy, low noise and high spatial resolution are important image quality parameters for treatment plan accuracy, determining their combined effect on the dosimetric accuracy requires elaborate consideration [11]. Investigations on the dosimetric accuracy of particle CT are limited to simulation studies (see, e.g., Meyer *et al.* [28]), and no in-tissue range accuracy test has yet been performed.

The purpose of the present work was to experimentally explore the range accuracy of HeCT compared to DECT, SECT and pCT by providing a clinical-like scenario using a post-mortem pig head in a bespoke phantom holder. To provide range accuracy in the context of image quality, RSP accuracy and spatial resolution of HeCT were also explored with dedicated CT QA phantoms.

2. Materials and Methods

2.1. Particle CT - Acquisition and reconstruction

To acquire HeCTs of the different phantoms, we utilized the US pCT collaboration prototype proton CT scanner [29] at the Heidelberg Ion-Beam Therapy Center (HIT) experimental cave [30]. The scanner prototype was originally designed and optimized for pCT studies at the Loma Linda University Medical Center Proton Treatment and Research Center and the Northwestern Medicine Chicago Proton Center. For the current experiment at HIT, we also acquired pCT scans with the scanner. A photograph and a schematic sketch of the experimental setup are shown in Figure 1.

The scanner comprises two tracking detectors, one preceding and one following the object in beam direction, measuring the position and direction for each particle. The particle's residual energy is measured by a 5-stage scintillator. Each stage of the scintillator is 50.8mm in thickness and read out by a single photomultiplier tube (PMT). In total, the energy/range detector covers a dynamic WET range of approximately 260mm. The field-of-view of the system is $360 \times 90\text{mm}^2$ (H×V). A remote-controlled rotating platform enables acquisition of CT scans, either in continuous or stepped scan mode. Further details on the prototype are published elsewhere, in particular in Johnson *et al.* [29] and Bashkirov *et al.* [31].

Helium ion and proton fields were delivered employing the HIT raster scanning method. The field size was $100 \times 200\text{mm}^2$ for the 150mm diameter phantoms, and $100 \times 250\text{mm}^2$ for the 200mm diameter phantom. The nominal beam energy was 200.11MeVu^{-1} for helium ions, and 200.38MeV for protons. The spot FWHM was 10.2mm for helium ions, and 12.8mm for protons. The lateral distance between adjacent spot centers was 3mm. Each field was delivered in a single spill of ~4s duration, and used for a single projection. The ~4s pause between spills was used to rotate the object. The particle rate was set to ~ 700kHz for helium ions, and ~ 1.35MHz for protons. Lowering the intensity further was not yet feasible for protons, due to limitations imposed by the HIT nozzle beam monitors that would prohibit raster scanning. Hence, ~2.8 and ~ 6.2 million events were irradiated for each projection for HeCT and pCT, respectively. Full HeCT scans were acquired from 360 projections, separated by 1° steps. For the tissue phantom (Section 2.4), the pCT scan was acquired from 180 projections due to beam time limitations. As a consequence of the spill structure, a 360 projection scan took a minimum of 48 minutes to complete.

The dose per scan can be estimated based on the simulation study by Piersimoni *et al.* [32], who, based on a digital version of the pCT prototype, simulated the dose delivered by a $150 \times 80\text{mm}^2$ homogeneous field of helium ions at 200MeV/u impinging on a water phantom of 80mm height and 150mm diameter. Considering the differences in the delivered number of particles and field size, the total absorbed dose to water was ~16mGy for the HeCT scan in our study. For the pCT with 180 projection and $\sim 6.2\times10^6$ particles per projection, the total absorbed dose to water was ~4.7mGy.

Prior to the scanning experiments, the detector response, measuring quenched scintillation light and being subject to PMT gain and noise pedestal variations, was calibrated to WET using a phantom setup of known geometry and RSP. In this prototype phase, the calibration needs to be performed once per experiment shift; using an older calibration would result in reduced accuracy due to differences in beam/detector setup [33]. Full details on the data acquisition, calibration and processing for this detector can be found in the report by Schultze *et al.* [34]. For helium ion imaging, the ΔE-E filter proposed by Volz *et al.* [27] was added to the data processing workflow.

Prior to image reconstruction, the particles were binned to $1 \times 1\text{mm}^2$ pixels projection-wise for applying 3-sigma filters on WET and angular displacement to remove noise events. For image reconstruction, the diagonally relaxed orthogonal row (DROP) block-iterative reconstruction method with interleaved superiorization of the total variation norm (TVS) [35] was applied. Particle paths were estimated using the optimized cubic spline path

formalism [36, 37]. A Feldkamp-David-Kress (FDK) cone beam filtered back projection was used as starting estimate for the iterative solver and to identify the object boundary for improved path estimation. All scans were reconstructed at $0.977 \times 0.977 mm^2$ pixel size and slice thickness of 2mm, in agreement with typical radiotherapy treatment planning voxel sizes. For the Catphan CTP404 phantom (Section 2.3.1) the DROP-TVS algorithm was run with a relaxation parameter of 0.1 and 40 optimization blocks as used by Giacometti *et al.* [38] for the same phantom, and the iterative solver was terminated after 50 iterations. For the spatial resolution (Section 2.3.2) and tissue phantom (Section 2.4), a relaxation parameter of 0.2 and 200 optimization blocks were used terminating the solver after 20 iterations, as found optimal for the spatial resolution phantom in [39].

2.2. X-ray CT - Acquisition and RSP conversion

SECT and DECT scans were acquired with a Siemens Somatom Definition Flash (Siemens Healthineers, Forchheim, Germany) dual-source scanner. To acquire SECT scans, the tube voltage was set to 120kV, the tube current time product to 215mAs and the field of view was 500mm. The scans were reconstructed using a H30s reconstruction kernel. For DECT acquisition, the two X-ray sources were run at voltages of 100kV and 140kV (tin filtered), respectively. Both tube current time products were 174mAs to keep the total image dose the same as for the SECT scan. Image reconstruction was done with a D34s reconstruction kernel. The $CTDI_{Vol,16\ cm}$ for SECT and DECT was 59mGy. These settings were established following a protocol to achieve high quality RSP images [12]. For all presented X-ray CTs, the slice thickness was 2mm and the pixel size was $0.977 \times 0.977 mm^2$.

For RSP calibration, we used scans of the Gammex RMI 467 electron density phantom (SunNuclear, Melbourne, FL, USA) acquired with the same SECT/DECT protocol. To convert the SECT to RSP, we employed the stoichiometric calibration method [2] which is the most widely used method in clinical practice [18]. RSP conversion from DECT was performed with the image based stoichiometric calibration method presented by Bourque *et al.* [7]. Further details on the RSP conversion from SECT and DECT as applied in this study are reported in our previous publication by Bär *et al.* [22]. Note that these conversion methods were initially proposed for proton therapy. However, due to the RSP being practically independent of ion type in the energy range used for treatment (especially when comparing protons and helium ions), a comparison to the HeCT predicted RSP is not relevantly affected by that.

2.3. Image quality

2.3.1. RSP accuracy - Catphan CTP404—A Catphan® (The Phantom Laboratories, Salem, NY, USA) CTP404 sensitometry module was used to assess the RSP accuracy of HeCT in order to validate the workflow for the experiments with the tissue sample. The phantom is an epoxy cylinder (RSP= 1.144±0.001) of 150mm diameter and 20mm height. It comprises six different cylindrical plastic inserts of 12mm diameter, placed at a radial position of 60mm. In detail, the samples are LDPE (RSP= 0.980 ± 0.002), Delrin (RSP= 1.359 ± 0.003), Teflon (RSP= 1.790 ± 0.002), PMP (RSP= 0.883 ± 0.002), Polystyrene (RSP= 1.024 ± 0.001), and PMMA (RSP= 1.160 ± 0.001). The stated reference RSP values

are measurements for this phantom acquired from carbon ion range pull-back measurements using the PEAKFINDER (PTW, Freiburg, Germany) water column [38].

The mean RSP ± standard deviation for the HeCT reconstructed images of the CTP404 sensitometry module was assessed in a cylindrical regions-of-interest (ROI) of 6mm diameter and 10mm height in the center of each of the inserts and compared to the reference values of Giacometti *et al.* [38]. We calculated the mean percentage error (MPE) of the insert RSPs, defined as $100 \times (RSP_{HeCT} - RSP_{ref})/RSP_{ref}$, of the inserts as well as the MAPE as the average of the absolute MPE of all inserts.

2.3.2. Spatial Resolution - CIRS custom phantom—A custom phantom designed by Plautz *et al.* [39] and custom manufactured by CIRS (Computerized Imaging Reference Systems Inc., Norfolk, Virginia) was used for investigating the spatial resolution of HeCT with an edge spread technique. It is a 200mm diameter cylindrical phantom of 60mm height made of CIRS Water-LR water equivalent plastic material (RSP=1.007) and comprises 9 rectangular inserts (edge length 15 × 15 × 45mm) made from tissue equivalent plastic materials: three model tooth enamel (RSP≈1.770), three cortical bone (RSP≈1.685) and three lung (RSP ≈ 0.217). In addition, three air gaps (RSP≈0.007) of the same dimension as the rectangular inserts are present in the phantom. The given RSPs were calculated from the material composition provided by the manufacturer because no measured values for the phantom were available. The inserts and air gaps were placed in the phantom at increasing radial distances (25mm, 55mm and 80mm) from the center and staggered around on the azimuth angle with 30-degree steps. A detailed schematic of the phantom can be found in Figure 1 in Plautz *et al.* [39].

The Modulation Transfer Function (MTF) for each cube in the phantom was computed using a slanted edge spread function technique. First, the oversampled edge spread function was acquired in an ROI around each cube edge in the central slice of the reconstructed CT scan. It was then fitted with an error function to suppress noise, as described in Gehrke *et al.* [20]. The Fourier transform of the derivative of the fit function yielded the MTF and the average MTF for each radial distance from the center was computed. The $MTF_{10\%}$ was used as the metric for comparison, as done in other works[40, 39].

2.4. Heterogeneous tissue sample

2.4.1. Pig head phantom—An animal tissue phantom was constructed to assess HeCT image quality and range prediction accuracy in a more clinically realistic scenario (see Figure 2). The phantom holder was a 3D-printed cylindrical container (150mm diameter 50mm height, 1mm wall thickness), with a central cylindrical compartment (30mm inner diameter, 1mm wall thickness), and made from VeroClear (Sculpteo, Villjuif, France) epoxy. Two fresh post-mortem pig head halfs were collected from a local butcher, and an approximately 40mm thick slice around the brain cavity of the cranium was sawed out from each half. The two slices were placed in the phantom container such that the central cylindrical compartment was located within the brain cavity of the cranium. The tissue was fixed in place with a 2% agarose-water gel mixture, ensuring that the liquid agarose-water mixture was cooled enough not to alter it. Small air enclosures, especially at the nasal

cavities, could not be avoided. The phantom was then sealed with a 3D printed lid, leaving access to the central cylindrical insert. The cylindrical insert, custom manufactured by CIRS from brain equivalent plastic, hosted a rectangular cavity ($10\times15\times30mm^3$; T×W×H) to hold a stack of radiosensitive films for range reference measurements. The final phantom is shown in Figure 2(a) and a slice of a SECT scan (in HU) is shown in Figure 2(b). HeCT/pCT scans and range reference measurements were acquired at night, the SECT/DECT scans were acquired the following midday. Between measurements, the phantom was stored in a fridge to avoid decay.

2.4.2. Range measurement—To acquire a range reference measurement within the phantom, we placed 36 ($(14.2 \pm 0.25) \times (29.4 \pm 0.25)mm^2$) Gafchromic™ EBT-XD radiosensitive films in the central compartment of the cylindrical insert. Each film had a physical thickness of 0.275mm as reported by the vendor[41]. We positioned the phantom such that the center of the film stack was in the laser isocentre and irradiated the setup with a proton pencil beam of 15.0mm FWHM at nominal initial energy of 105.43MeV (84.67mm range in water) in 5 full spills at a beam intensity of 4×10^8protons/s. A proton beam was chosen to keep dose response quenching in the films to a minimum; The energy of the proton beam was set to approximately place the proton Bragg peak in the film stack center. To assess the reproducibility of the experimental results, we performed two independent film experiments.

We scanned the films with an Epson Expression 10000XL (Epson, Suwa, Japan) scanner six days after the irradiation. Each film was kept individually in a closed envelope in a light tight drawer between irradiation and scan. To evaluate the scans, we followed the procedure by Martisikova and Jäkel [42]: first, we evaluated the mean pixel value (PV) in the red color channel of an unirradiated film kept alongside the irradiated ones in a central rectangular ROI of $11 \times 26mm^2$. In the same way, we evaluated the PV for each of the 36 irradiated films. In addition, we acquired a background (BG) image of the scanner. The net optical density (nOD) of film $i \in \{1 \ldots 36\}$ was calculated as:

$$\mathrm{nOD}_i = \log\left(\frac{\mathrm{PV}_{unirr.} - \mathrm{PV}_{BG}}{\mathrm{PV}_i - \mathrm{PV}_{BG}}\right) \quad (1)$$

To calibrate the dose response, we irradiated reference films from the same batch with $40\times40mm^2$ homogeneous fields of 105.43MeV protons. The doses to the films were approximately 1.5Gy, 3Gy, 6Gy and 12Gy. The films' nOD was evaluated as above, and an nOD-to-dose calibration function was derived as described by the EBT-XD user manual[41]. No additional correction for quenching effects was performed. The film RSP was estimated from HeCT to be 1.231±0.002, where the uncertainty refers to the standard error of the mean.

2.4.3. Registration—For comparing the CT scans of the tissue phantom, 3D-3D rigid registration was performed. For that, the RSP converted SECT and DECT scans were registered onto the HeCT reconstructed scan of the tissue phantom using the 3DSlicer[43] toolkit (www.slicer.org) based on image intensity.

2.4.4. Monte Carlo simulated range—To evaluate the accuracy of HeCT based range prediction against the other modalities, we conducted Monte Carlo simulations of the setup with the Geant4 particle transport toolkit [44] (v10.2-p.3). For each modality, the registered RSP scans (see Section 2.4.3) were used to create a voxelized phantom geometry utilizing the *G4PhantomParametrization* class provided by the Geant4 toolkit. The CT geometry was modeled as water with density adjusted to the voxel RSPs (water elemental composition from NIST database [45], and ionization potential of 78eV following recent recommendations [46]). In addition to the phantom, the HIT beam monitoring system and the air between nozzle and isocenter were considered in the simulation in the form of a slab of 3.05mm WET [47]. To match the experimental conditions of the Gafchromic film measurement (see Section 2.4.2), the proton beam was generated as a Gaussian pencil beam of 15.0mm FWHM and 105.43MeV initial energy (monoenergetic) directly at the entrance of the nozzle water slab. For each run, 10^5 primary protons were simulated. The following physics lists were active in the simulation: *G4EMStandard_option4* and *G4EMExtraPhysics* for accurate modelling of electromagnetic processes, *G4HadronElasticPhysics*, *G4HadronPhysicsQGSP_BIC_HP* and *G4IonBinaryCascadePhysics* to model elastic and inelastic nuclear interactions, *G4DecayPhysics* and *G4RadioactveDecayPhysics* to model particles and their decay, and *G4StoppingPhysics* to model nuclear capture at rest. A step limit of 0.1mm was set within the voxelized geometry, and production cuts (affecting electrons and photons) were set to 0.5mm.

In the simulation, the energy deposit of the particles in the film stack was scored in an ROI of 11mm width, 26mm height and 9.9mm thickness, and binned to a 1-D histogram (0.275mm bin width) along the beam direction. The ROI was placed such that its entrance coincided with the edge of the first pixel row corresponding to the film stack in the CT scan. In addition, we recorded the dose to each CT voxel to compare the predicted proton dose distribution for the different CT modalities.

2.4.5. Range estimation uncertainty budget—The alignment of the ROI for range evaluation in simulation and the actual position of the film stack is subject to an uncertainty of half the CT voxel dimension, i.e., ~ 0.5mm×RSP_{films} in the beam direction. In addition, the WET of the nozzle and air to isocenter is subject to an uncertainty of ±0.1mm [48]. Finally, range variations from accelerator fluctuations can occur, with reference measurement from our center quoting a systematic offset of 0.3mm. While we corrected the analysis for this systematic offset, a ±0.3mm uncertainty is included in the uncertainty of the reference measurement to acknowledge potential fluctuations. Additional uncertainty resides in estimating the films' RSP through HeCT. This is negligible, however, due to the small thickness of the film stack: Even a 1% systematic error would result in less than 0.1mm uncertainty of the total WET of the stack. The overall uncertainty of the reference measurement was determined to be ±0.69mm by quadratically adding the above uncertainty sources. To estimate the uncertainty resulting from positioning of the phantom, for each modality, we repeated the range simulations for ±1mm lateral translations (horizontal and vertical) and ±1° rotations (horizontal). A min/max region around the range estimate for each modality was then determined from the seven simulations.

3. Results

3.1. RSP accuracy

Figure 3(a) shows a slice of the reconstructed experimental HeCT of the Catphan® CTP404 sensitometry module. Figure 3(b) shows the RSP accuracy. For each insert the MPE was better than 1%. The MAPE over all inserts was 0.30% with standard error of the mean being 0.1%. The average standard deviation in the insert ROIs, representing the inter-pixel noise, was 0.37%. A detailed investigation of the RSP accuracy as function of dose, number of projections, and DROP-TVS parameters is provided in Appendix A.

3.2. Spatial resolution

Figure 4 shows a HeCT reconstructed slice of the custom spatial resolution phantom. The $MTF_{10\%}$ was 5.9±0.4lp/cm for the central, 7.5±0.4lp/cm for the middle, and 7.6 ± 0.8lp/cm for the peripheral cubes, where the given uncertainty corresponds to the standard deviation of the $MTF_{10\%}$ estimates from the four cubes. For comparison, the spatial resolution of the DECT scan acquired with clinical settings was 7.7±0.3lp/cm for the center, 7.6±0.2lp/cm for the middle and 7.4±0.2lp/cm for the peripheral cubes.

3.3. Heterogeneous tissue sample

Figure 5 depicts HeCT, DECT, SECT and pCT reconstructed slices of the custom pig-head phantom. Visually, all four modalities performed similarly. Note that the pCT scan was acquired from 180 projections at 2° steps, in contrast to the 360 projections available for HeCT. A HeCT reconstruction from only 180 out of the available 360 projections for better comparison with the pCT scan is provided in Appendix B.

Figure 6 presents line profiles through each of the reconstructed CT slices shown in Figure 5. HeCT and DECT reconstructions agree with each other, although DECT depicts some noise spikes. SECT gives similar results in soft tissues compared to HeCT, but much larger values for bones, and significantly lower RSP for the central film inserts. pCT is similar to HeCT, but cannot resolve small bone features for which it produces smaller RSP when compared to HeCT or DECT. This limitation is related to the protons' scattering as well as the limited angle reconstruction.

Figure 7 shows the relative percentage difference in RSP between HeCT and the other modalities after rigid registration. The selected slice is the same as that shown in Figure 5. For each voxel, the percentage difference was calculated as $(RSP_{HeCT} - RSP_x)/(RSP_{HeCT})$, where x stands for each of the other three modalities. For better comprehensiveness of the difference maps, the air and the phantom holder (for the photon based modalities) outside a 75mm radius from the center were masked.

The comparison to DECT shows slightly lower mean RSP values in HeCT, with the mean percentage difference ± standard deviation in a central cylindrical ROI of 60mm radius and 8mm height, i.e., representing the heterogeneity of the phantom, being (−0.40 ± 8.34)%. Compared to pCT, HeCT reconstructs slightly larger RSP values, at a mean percentage difference of (0.37±6.05)%. The largest difference was observed comparing HeCT to SECT.

Here, large relative differences exceeding several percent were present in small cortical bone features, with the mean difference being (−2.25 ± 9.2)%. Moreover, the difference map shows a tendency for overestimated RSP values in SECT towards the phantom periphery, which is likely due to beam hardening. Larger relative errors are also present at air gaps, where even small absolute differences in RSP result in comparatively large relative errors due to the small RSP of air. In all three difference maps, rings in the relative difference can be seen, albeit most prominently in the HeCT-pCT difference map, corresponding to ring artefacts present in the particle CT image reconstructions.

3.4. Range accuracy

Figure 8a) shows the simulated dose of the proton pencil beam overlayed on the HeCT reconstruction of the pig head sample. The dose was normalized to the pencil beam peak dose. Figure 8b)–d) shows the difference of the dose estimates in percent based on HeCT and that of DECT, SECT and pCT, respectively, relative to the HeCT based simulated peak dose of the proton pencil beam. Comparing HeCT and DECT, dose differences in the distal fall-off of the pencil beam can be seen, indicating a slightly lower range for the DECT based simulation. For both SECT and pCT, larger dose differences were observed over the full distal falloff of the proton pencil beam. For SECT, the differences indicate an undershoot, for pCT an overshoot compared to HeCT.

Figure 9 shows a comparison of the depth-dose profile between prediction from the simulations based on each CT modality and the dose recorded by the EBT-XD films. Peak-to-peak distances were measured on a WET scaled range, where simulated depth-dose profiles were scaled by the film RSP found within the respective modality, and the reference was scaled by the HeCT determined RSP. The gray shaded region around the film measured depth-dose profile indicates the WET uncertainty from the uncertainty budget considerations (see Section 2.4.5). The error bars of the reference measurement indicate the difference between the two individual measurements used to generate the reference curve. The shaded areas around the simulated depth-dose profiles indicate the min/max region for all simulations performed considering potential lateral/rotational misalignment.

The observed peak-to-peak distance was (−0.22±0.15)mm WET for the HeCT proton pencil beam simulation, (−0.38±0.25)mm WET for DECT, (0.33±0.16)mm WET for pCT and (−1.19 ± 0.20)mm WET for SECT. The given uncertainty corresponds to the standard deviation of the peak-to-peak distances obtained from the budget uncertainty simulations (Section 2.4.5). Relative to the proton beam range, the observed peak-to-peak distances correspond to a percentage range accuracy of (−0.25 ± 0.18)% (HeCT based), (−0.45 ± 0.29)% (DECT based), (0.39 ± 0.19)% (pCT based) and (−1.40 ± 0.24)% (SECT based). In terms of the 80% fall off, the relative differences were (−0.29±0.14)% for HeCT, (−0.46±0.16)% for DECT, (0.39 ± 0.13)% for pCT and (−1.47 ± 0.12)% for SECT. The differences between HeCT, DECT and pCT compared to the film measured range were within the experimental uncertainty.

4. Discussion

In this work, we presented an analysis of the image quality and range accuracy achievable with helium ion imaging. Two plastic phantoms enabled us to assess and quantify RSP accuracy and spatial resolution. A custom animal tissue phantom allowed us to explore the image quality of HeCT in a fully clinically realistic case and enabled a proof-of-concept range accuracy comparison to pCT, SECT and DECT.

4.1. Image quality of HeCT

The HeCT RSP accuracy for the CTP404 sensitometry module was demonstrated to be (0.30 ± 0.37)% in this work, slightly better than what we reported in our previous work on helium imaging [27], where the HeCT acquisition was limited to 90 projections. We find the RSP accuracy and noise to depend not only on dose, but also on the specific DROP-TVS reconstruction parameters used, where in general, a larger image dose (i.e., more recorded events) required more iterations for the solver to converge for otherwise equal reconstruction parameters. Especially, we found the previously reported number of iteration (8 in Giacometti *et al.*[49]) to correspond to a maximum in MAPE, but a minimum in the image noise for the Catphan CTP404 phantom (see Appendix A). Since the convergence of the iterative solver is central to the accuracy/precision of reconstructed RSP values, as also noted by Hansen *et al.* [50], further optimization of the DROP-TVS parameters may lead to further image quality improvements. Such an optimization was, however, out of the scope of the present work.

The spatial resolution of the HeCT was found comparable to that of the treatment planning DECT scan (Figure 4). Only in the center of the 20cm diameter phantom, where the path estimation uncertainty is largest, the spatial resolution was somewhat reduced. With an ideal tracking geometry, the maximum uncertainty in the path estimation would reach up to ~0.25mm for 200MeV/u helium ions traversing 20cm of water. This would correspond to a theoretical spatial resolution limit of approximately 10lp/cm [21]. As this is above the limitation arising from the applied ~1mm pixel size, one would in principle expect the spatial resolution for HeCT to be the same everywhere in the phantom. The reduced spatial resolution in the phantom center for HeCT in this work may be explained from the uncertainty of the tracker system, and the distance between the trackers and the phantom, as this is known to negatively influence the path estimation [51]. Moreover, similar to the discussion above, the spatial resolution is subject to the DROP-TVS reconstruction parameters, and further optimization might be possible.

4.2. Heterogeneous tissue phantom

An important and novel aspect of this study was the range accuracy achievable with HeCT in clinically realistic heterogeneous tissue phantom. For the heterogeneous tissue phantom, HeCT provided a similar visual image quality compared to SECT and DECT, which will make the application in clinical routine straightforward. It is necessary to keep in mind that the contrast of particle CT is that of the tissue RSP, which lacks the relatively large contrast between bone and soft tissue of X-ray based CT modalities.

Quantitatively, differences between the HeCT reconstructed RSP and that of the other modalities were similar to what has been observed in our previous work on individual homogeneous tissue samples in our companion study [22]. In the current work, the range prediction based on HeCT achieved high accuracy, with a peak-to-peak distance of −0.25 ± 0.18% compared to the reference measurement. This was slightly better than pCT and DECT, which yielded a peak-to-peak accuracy of 0.39±0.19% and −0.45±0.29%, respectively. The distal dose falloff predicted by pCT most closely resembled the film measurement. It has to be mentioned that there are LET-dependent quenching effects in the film dose response, which increase towards the end of the range of the protons, resulting in an underestimation of the peak dose. Since the peak dose was used for normalization of the curves, the dose in the plateau is slightly higher in the film measurement compared to the simulated dose. Overall, HeCT, DECT, and pCT achieved better than 1mm accuracy, within the range uncertainty accepted anyways for accelerator quality assurance measurements. The observed differences would thus not be clinically relevant. SECT had the largest range prediction error with a peak-to-peak distance at −1.19 ± 0.20mm, −1.40 ± 0.24% relative to the total range of the beam.

These results are in-line with the expectation from the recent literature comparing particle and X-ray modalities in terms of stopping power prediction [16, 22], and dosimetric accuracy in a simulation study [28]. The lower accuracy of SECT was discussed more than 20 years ago in the study by Schaffner *et al.* [3]. Noteworthy, the pig-head featured thicker cranial bone when compared to the human skull. As SECT based RSP prediction is worst for bone tissue [22], the range uncertainty of SECT based range prediction might be overestimated compared to the clinical case. On the other hand, while the investigated ~ 85mm range represents a clinically realistic treatment depth (e.g. for head-and-neck patients), a significant portion of patients is treated for deeper seated tumors (e.g. prostate). For these, differences in RSP accuracy can lead to larger range differences, and the use of a more advanced RSP estimation modality is favored.

As a caveat, this study represents a single sampling of range prediction from the different systems, as it was based on a single tissue phantom. More biological sample phantoms at varying size and composition are needed to support a resilient conclusion on the usefulness of HeCT compared to the other modalities. Still, the results here provide a proof-of-concept that HeCT (and also pCT) acquired with an experimental prototype scanner can yield an image quality and range prediction accuracy comparable to that of DECT acquired with a commercial X-ray CT system certified and maintained as a medical product.

4.3. Image dose

All presented HeCT scans in this work were acquired from 360 projections at ~ 2.8×10^6 particles/projection. Based on the simulation study by Piersimoni *et al.* [32], the absorbed dose to water was ~16mGy. The pCT scan acquired from 180 projections at ~ 6.2×10^6 particles/projection the absorbed dose to water was ~4.7mGy. This is a low dose compared to the $CTDI_{Vol,16\ cm}$ dose quoted for both SECT and DECT of 59mGy. Still, both values are larger than the dose for pCT reported in the literature, and this has to be considered when comparing our data to previous studies. For example, Dedes *et al.* [16] report a dose

of 2mGy for pCT scans of plastic phantoms with RSP accuracy slightly better than that of DECT. The higher dose delivered for the HeCT and pCT scans in our study was due to the relatively high dose per projection. This resulted from the chosen field parameters at the HIT facility, where raster scanning was not designed for the low fluence operation required for dose-efficient particle CT. The beam monitoring system limits the minimal beam current and the minimum number of particles deliverable per beam spot. This is, however, not a general limitation, and further optimization of the raster scanning beam delivery for low fluence imaging would enable lower imaging doses, e.g. by lowering the number of beam spots to cover the imaging field.

4.4. Imaging limitations and artefacts

In our study, HeCT suffered from image reconstruction artefacts related to the current US collaboration scanner prototype. Ring-like artefacts in the reconstructions are a known problem with the system. They result from the WEPL calibration procedure not working optimally at the stage interfaces of the 5-stage multistage detector. This issue has been investigated in detail already elsewhere [52, 16] and an empirical correction method has been proposed recently by Dickmann *et al.* [33]. Interestingly, ring artefacts were smaller in amplitude for HeCT compared to what has been observed for pCT. This could give additional insight into the origin of such artefacts and is currently being investigated as part of a technical comparison between helium ion and proton imaging with the detector.

In addition to the ring artefacts mentioned above, HeCT reconstructions of the spatial resolution phantom (Figure 4) also presented a central overestimation of RSP. This is related to the particles crossing the thickest part of the phantom (~20cm WET) stopping in the very first detector stage. Since using a ΔE-E filter to remove secondary fragments requires the particles to have crossed at least into the second stage of the detector, the artefact is likely attributed to the lack of fragment filtering for particles stopping in the first stage. In order to achieve accurate HeCT over the full dynamic range of the prototype (260mm WET), a small ΔE stage would need to be added upstream of the energy detector. In that regard, it is important to note that although the ΔE-E filter has been shown in simulations to also improve pCT [53], it was not applied to the pCT scan shown in this work. While it removed a similar nuclear interaction background as in simulation, we recently observed a slight decrease in RSP accuracy by using the filter [22].

The limitations mentioned above are introduced by the current prototype scanner, which was optimized for proton imaging rather than imaging with helium ions. Further optimization of the energy detector for helium ions may, therefore, further improve image quality. Moreover, it has to be mentioned that DECT also suffers from limitations. For DECT, the chosen RSP conversion method uses phenomenological fits to create a non-physical relationship between mass attenuation, elemental composition and RSP. As such, any material that falls outside the calibration region will suffer from extrapolation artefacts. This can be seen, for example, for the tooth enamel cubes (Figure 4), where the large difference in RSP (1.853 for DECT vs 1.770 reference) is most likely attributed to the poor representation of human tissues offered by the CIRS enamel plastic composition[18] and the fact that the DECT RSP calibration was

tuned for human tissue. HeCT, as a direct method to retrieve the RSP, does not suffer from such issues.

4.5. Future clinical perspective

The similarity in performance of HeCT, DECT and pCT brings up the question of whether one should use HeCT in clinical applications at ion therapy centers. Compared to DECT, the major advantage of particle CT, in general, is reducing image dose to the patient. Although dose reduction might also be possible with iterative algorithms in DECT [6], the dose advantage of particle CT can still be significant for frequent imaging in adaptive therapy and especially beneficial for pediatric patients. Moreover, particle CT presents a direct method for RSP reconstruction, which would be advantageous for patients with metallic implants[17]. These advantages, however, are provided by both pCT and HeCT, with pCT offering an additional dose advantage [21]. The reasoning for HeCT resides in the improved spatial resolution, which is comparable to the resolution of X-ray CT[21]. Having similar range prediction accuracy, it is unclear whether the spatial resolution benefit of HeCT would provide a significant therapeutic benefit over pCT. In the simulation study by Meyer et al. [28], HeCT and pCT performed similarly regarding dosimetric accuracy. Still, the improved spatial resolution of HeCT may be advantageous in certain cases where the treatment field is passing along high RSP gradient edges. The possible benefit of HeCT should therefore be further investigated for different treatment sites in the future. There is an increasing interest in helium ion therapy[54, 55], with clinical implementation currently ongoing at HIT [56], for which HeCT could be of particular interest. It is important to note that the RSP of materials is independent of ion type, and HeCT, for example, would also benefit proton therapy in clinical practice, particularly if both ions are available in the same center. HeCT thus remains an attractive option for treatment planning for proton, helium and carbon ion therapy.

The main hurdle for clinical HeCT is the long scanning time for a full HeCT scan. For pCT at a cyclotron facility with uninterrupted data acquisition, a planning CT scan takes approximately six minutes with the US pCT prototype [29]. Ongoing efforts on detector developments [57, 58, 59] aim at an acquisition time of just 1 or 2 minutes in the near future. In order to enable continuous data acquisition for patient scans, either a rotating chair or a gantry capable of continuous irradiation during rotation is needed. Suitable chair systems have been installed, e.g. at the Shanghai Proton and Heavy Ion Center [60] and the Northwestern Medicine Chicago Proton Center (Warrenville, IL, USA). Recent work has demonstrated the first proof of continuous irradiation during gantry rotation in the context of proton arc therapy[61]. At a synchrotron facility, currently the only option for HeCT, the beam delivery pauses a few seconds between spills, greatly increasing the scan acquisition time. But optimized beam delivery and image acquisition techniques could keep spill pauses to a minimum. Of note, due to the better noise properties of helium ions compared to protons [20, 21], for equal particle acquisition rate, shorter beam on time would be sufficient to provide the data for a HeCT scan of the same noise quality as a pCT scan.

Using HeCT as an independent method for treatment planning would require an extra planning session for the patient in the treatment room. Considering the tight economic

constraints placed on particle therapy facilities, it is an open question if this would be feasible for every patient. On the other hand, helium ion radiographies could be acquired in few seconds with existing equipment. In clinical practice, one could use DECT to generate the treatment plan, and helium or proton radiography for independent verification and patient specific optimization of the CT calibration [62]. This may currently be the most practical use of helium ions for imaging. HeCT (or pCT) could be reserved for selected cases, e.g., pediatric cases, patients with metal implants, or cases where the beam stops near an organ at risk. The potential of HeCT for heterogeneous geometries demonstrated in this work suggests that it could also be used as an independent quality assurance tool for SECT/DECT-based treatment planning.

5. Conclusion

This work presents an evaluation of the spatial resolution and RSP accuracy possible with HeCT acquired with a prototype scanner. In addition, a first evaluation of the accuracy of HeCT based range prediction in a heterogeneous tissue phantom has been provided. Results were compared to SECT, DECT and pCT, where HeCT showed an overall promising potential. Offering a spatial resolution and range accuracy comparable to that of DECT at lower image dose and without the need for empirical conversion methods, HeCT remains an attractive option for future particle therapy treatment planning. Technological improvements are still needed to reduce scan acquisition times and to enable clinical implementation.

Acknowledgements

We thank the Heidelberg Ion-Beam Therapy Center for providing the beam time and support during measurements. We acknowledge Northern Illinois University (DeKalb) and especially George Coutrakon for lending us the CIRS brain equivalent plastic insert for range reference measurement inside the tissue phantom. Esther Bär is supported by the Radiation Research Unit at the Cancer Research UK City of London Centre Award C7893/A28990. Charles-Antoine Collins-Fekete is supported by a UKRI Future Leaders Fellowship No. MR/T040785/1. The authors gratefully acknowledge project funding through the Particle Therapy Co-Operative Group (PTCOG). The authors gratefully acknowledge the support of the National Institute of Biomedical Imaging and Bioengineering (NIBIB) of the National Institute of Health (NIH) and the National Science Foundation (NSF) award number R01EB013118, and the United States - Israel Binational Science Foundation (BSF) grant no. 2013003.

Appendix A.: Convergence of the iterative particle CT reconstruction algorithm

Figure A1(a) shows the convergence of the MAPE with the number of DROP-TVS iterations for different image dose and number of projections, at otherwise equal reconstruction parameters (same as used for the phantom in the main text). The 180 projections and 90 projections represent reconstructions when using only every second or fourth projection from the data. The label ‘dose norm.’ indicates reconstructions normalized to the dose of the 90 projection scan by randomly removing 75% and 50% of the recorded events for each of the 360 and 180 projection reconstructions, respectively. For the same settings, figure A1(b) depicts the standard deviation of the percentage RSP error averaged over all inserts in the phantom. It can be seen that for higher imaging doses, a low number of iterations produces an increased MAPE, and convergence settles later compared to lower imaging doses. The reconstruction from 90 projections returned the overall lowest MAPE. However, the low dose reconstructions also come at the highest noise.

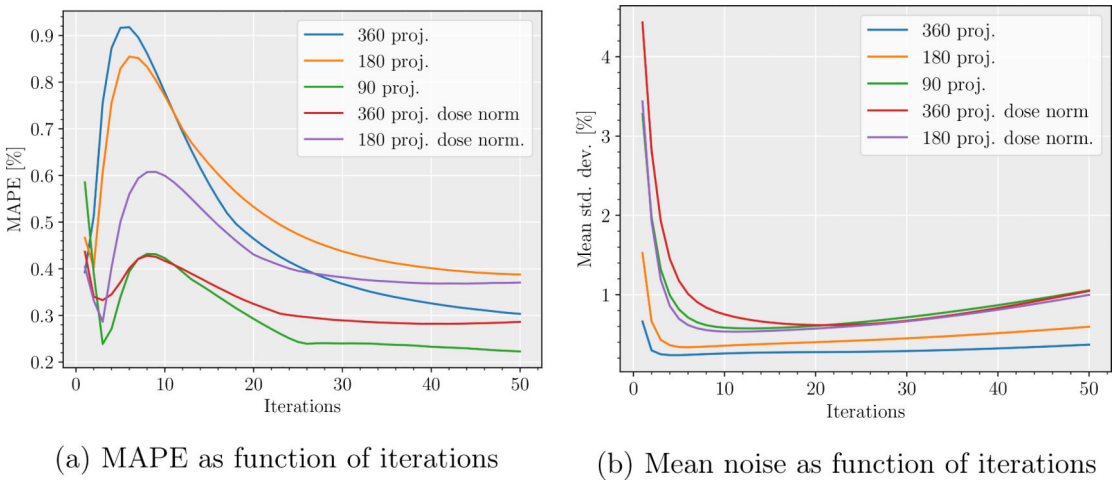

(a) MAPE as function of iterations (b) Mean noise as function of iterations

Figure A1:

a) Mean absolute percentage error of the HeCT reconstructed image of the CTP404 module as function of number of projection (90, 180, 360) used to reconstruct the scan, dose (full dose or dose-normalized to the 90 projection scan, denoted dose norm.), and number of iterations of the DROP-TVS iterative reconstruction algorithm. b) Same for the mean standard deviation of the RSP error for the inserts.

Appendix B.: Comparison of pCT and HeCT at equal number of projections

Figure B1(a) shows a comparison between pCT and HeCT reconstructed slices of the tissue phantom, where the HeCT was reconstructed from only 180 out of the 360 acquired projections at the same reconstruction parameters as in the main text. Figure B1(b) shows a central line profile through the reconstructed slices in Figure B1(a) as indicated by the horizontal lines. The use of fewer projection angles for HeCT resulted in increased noise, but the reconstructions still yielded an advantage in visual spatial resolution, visible, e.g., at bone structures. It has to be noted, that due to the DROP-TVS algorithm's convergence depending on the number of events as shown in Appendix A, different DROP-TVS parameters may be better suited for the reconstruction of the 180 projection HeCT, possibly improving image noise.

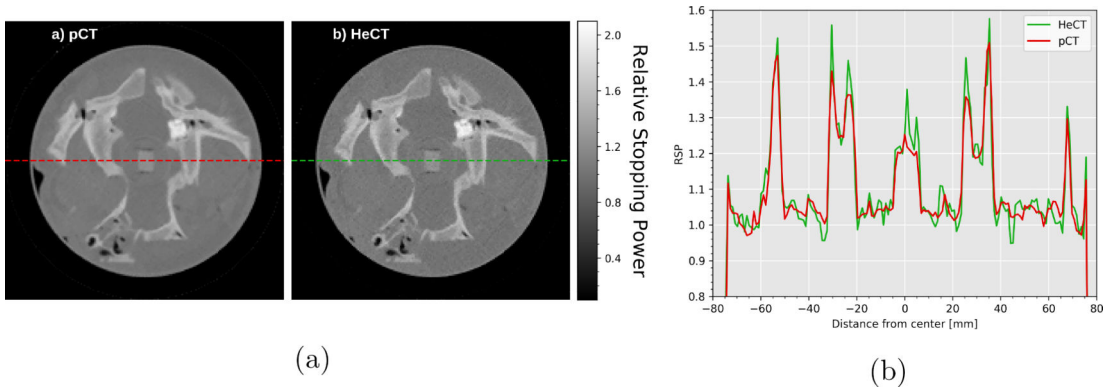

(a) (b)

Figure B1:

a) Comparison of pCT and HeCT of the tissue phantom, where the HeCT was reconstructed from only 180 out of the 360 projections. The voxel size in both cases was $0.97\times0.97\times2mm^3$, and the same DROP-TVS parameters as used for the reconstruction of this phantom in the main text were chosen. b) Comparison of the central line profiles.

References

[1]. Paganetti H, Range uncertainties in proton therapy and the role of Monte Carlo simulations, Physics in Medicine and Biology 57, R99 (2012). [PubMed: 22571913]

[2]. Schneider U, Pedroni E, and Lomax A, The calibration of CT Hounsfield units for radiotherapy treatment planning, Physics in medicine and biology 41, 111 (1996). [PubMed: 8685250]

[3]. Schaffner B and Pedroni E, The precision of proton range calculations in proton radiotherapy treatment planning: experimental verification of the relation between CT-HU and proton stopping power, Physics in Medicine and Biology 43, 1579–1592 (1998). [PubMed: 9651027]

[4]. Yang M, Zhu XR, Park PC, Titt U, Mohan R, Virshup G, Clayton JE, and Dong L, Comprehensive analysis of proton range uncertainties related to patient stopping-power-ratio estimation using the stoichiometric calibration, Physics in Medicine and Biology 57, 4095–4115 (2012). [PubMed: 22678123]

[5]. Lomax AJ, Myths and realities of range uncertainty, The British Journal of Radiology 93, 20190582 (2020), [PubMed: 31778317]

[6]. Wohlfahrt P and Richter C, Status and innovations in pre-treatment CT imaging for proton therapy, The British Journal of Radiology 93, 20190590 (2020), [PubMed: 31642709]

[7]. Bourque AE, Carrier J-F, and Bouchard H, A stoichiometric calibration method for dual energy computed tomography, Physics in Medicine and Biology 59, 2059 (2014). [PubMed: 24694786]

[8]. Taasti VT, Petersen JBB, Muren LP, Thygesen J, and Hansen DC, A robust empirical parametrization of proton stopping power using dual energy CT, Medical Physics 43, 5547–5560 (2016). [PubMed: 27782721]

[9]. Möhler C, Wohlfahrt P, Richter C, and Greilich S, Range prediction for tissue mixtures based on dual-energy CT, Physics in medicine and biology 61, N268–N275 (2016). [PubMed: 27182757]

[10]. Wohlfahrt P, Möhler C, Hietschold V, Menkel S, Greilich S, Krause M, Baumann M, Enghardt W, and Richter C, Clinical Implementation of Dual-energy CT for Proton Treatment Planning on Pseudo-monoenergetic CT scans, International Journal of Radiation Oncology*Biology*Physics 97, 427–434 (2017).

[11]. Bär E, Lalonde A, Royle G, Lu H-M, and Bouchard H, The potential of dual-energy CT to reduce proton beam range uncertainties, Medical Physics 44, 2332–2344 (2017). [PubMed: 28295434]

[12]. Bär E, Lalonde A, Zhang R, Jee K, Yang K, Sharp G, Liu B, Royle G, Bouchard H, and Lu H, Experimental validation of two dual-energy CT methods for proton therapy using heterogeneous tissue samples, Medical Physics 45, 48–59 (2018). [PubMed: 29134674]

[13]. Möhler C, Russ T, Wohlfahrt P, Elter A, Runz A, Richter C, and Greilich S, Experimental verification of stopping-power prediction from single- and dual-energy computed tomography in biological tissues, Physics in Medicine & Biology 63, 025001 (2018). [PubMed: 29239855]

[14]. Taasti VT, Michalak GJ, Hansen DC, Deisher AJ, Kruse JJ, Krauss B, Muren LP, Petersen JBB, and McCollough CH, Validation of proton stopping power ratio estimation based on dual energy CT using fresh tissue samples, Physics in Medicine & Biology 63, 015012 (2017). [PubMed: 29057753]

[15]. Schulte R, Bashkirov V, Li Tianfang, Liang Zhengrong, Mueller K, Heimann J, Johnson L, Keeney B, Sadrozinski H-W, Seiden A, Williams D, Zhang Lan, Li Zhang, Peggs S, Satogata T, and Woody C, Conceptual design of a proton computed tomography system for applications in proton radiation therapy, IEEE Transactions on Nuclear Science 51, 866–872 (2004).

[16]. Dedes G, Dickmann J, Niepel K, Wesp P, Johnson RP, Pankuch M, Bashkirov V, Rit S, Volz L, Schulte RW, Landry G, and Parodi K, Experimental comparison of proton CT and dual energy x-ray CT for relative stopping power estimation in proton therapy, Physics in Medicine & Biology 64, 165002 (2019). [PubMed: 31220814]

[17]. Civinini C, Scaringella M, Brianzi M, Intravaia M, Randazzo N, Sipala V, Rovituso M, Tommasino F, Schwarz M, and Bruzzi M, Relative stopping power measurements and prosthesis artifacts reduction in proton {CT}, Physics in Medicine & Biology 65, 225012 (2020). [PubMed: 33200747]

[18]. Gomà C, Almeida IP, and Verhaegen F, Revisiting the single-energy CT calibration for proton therapy treatment planning: a critical look at the stoichiometric method, Physics in Medicine & Biology 63, 235011 (2018). [PubMed: 30474618]

[19]. DeJongh DF, DeJongh EA, Rykalin V, DeFillippo G, Pankuch M, Best AW, Coutrakon G, Duffin KL, Karonis NT, Ordoñez CE, Sarosiek C, Schulte RW, Winans JR, Block AM, Hentz CL, and Welsh JS, A Comparison of Proton Stopping Power Measured with Proton CT and X-Ray CT in Fresh Post-Mortem Porcine Structures, 2020.

[20]. Gehrke T, Amato C, Berke S, and Martišíková M, Theoretical and experimental comparison of proton and helium-beam radiography using silicon pixel detectors, Physics in Medicine & Biology 63, 035037 (2018). [PubMed: 29311417]

[21]. Collins-Fekete C-A, Dikaios N, Bär E, and Evans PM, Statistical limitations in ion imaging, Physics in Medicine & Biology (2021).

[22]. Bär E, Volz L, Collins-Fekete C-A, Brons S, Runz A, Schulte R, and Seco J, Experimental comparison of photon versus particle computed tomography to predict tissue relative stopping powers, (2021), Submitted to and under review by Medical Physics.

[23]. Gehrke T, Gallas R, Jäkel O, and Martišíková M, Proof of principle of helium-beam radiography using silicon pixel detectors for energy deposition measurement, identification, and tracking of single ions, Medical Physics, n/a–n/a (2017).

[24]. Amato C, Martisikova M, and Gehrke T, A technique for spatial resolution improvement in helium-beam radiography, Medical Physics 47, 2212–2221 (2020). [PubMed: 31995641]

[25]. Kopp B, Meyer S, Gianoli C, Magallanes L, Voss B, Brons S, and Parodi K, Experimental comparison of clinically used ion beams for imaging applications using a range telescope, Physics in Medicine & Biology 65, 155004 (2020). [PubMed: 32268309]

[26]. Volz L, Collins-Fekete C-A, Piersimonii P, Johnson RP, Bashkirov V, Schulte R, and Seco J, Stopping power accuracy and spatial resolution of helium ion imaging using a prototype particle CT detector system, Current Directions in Biomedical Engineering 3, 401–404 (2017).

[27]. Volz L, Piersimoni P, Bashkirov VA, Brons S, Collins-Fekete C-A, Johnson RP, Schulte RW, and Seco J, The impact of secondary fragments on the image quality of helium ion imaging, Physics in Medicine & Biology 63, 195016 (2018). [PubMed: 30183679]

[28]. Meyer S, Kamp F, Tessonnier T, Mairani A, Belka C, Carlson DJ, Gianoli C, and Parodi K, Dosimetric accuracy and radiobiological implications of ion computed tomography for proton therapy treatment planning, Physics in Medicine & Biology 64, 125008 (2019). [PubMed: 30870831]

[29]. Johnson RP, Bashkirov V, DeWitt L, Giacometti V, Hurley RF, Piersimoni P, Plautz TE, Sadrozinski HF-W, Schubert K, Schulte R, Schultze B, and Zatserklyaniy A, A Fast Experimental Scanner for Proton CT: Technical Performance and First Experience With Phantom Scans, IEEE transactions on nuclear science 63, 52–60 (2016). [PubMed: 27127307]

[30]. Haberer T, Debus J, Eickhoff H, Jäkel O, Schulz-Ertner D, and Weber U, The heidelberg ion therapy center, Radiotherapy and Oncology 73, S186–S190 (2004). [PubMed: 15971340]

[31]. Bashkirov VA, Johnson RP, Sadrozinski HF-W, and Schulte RW, Development of proton computed tomography detectors for applications in hadron therapy, Nuclear Instruments & Methods in Physics Research. Section A, Accelerators, Spectrometers, Detectors and Associated Equipment 809, 120–129 (2016).

[32]. Piersimoni P, Faddegon BA, Méndez JR, Schulte RW, Volz L, and Seco J, Helium CT: Monte Carlo simulation results for an ideal source and detector with comparison to proton CT, Medical Physics 0 (2018).

[33]. Dickmann J, Sarosiek C, Götz S, Pankuch M, Coutrakon G, Johnson RP, Schulte RW, Parodi K, Landry G, and Dedes G, An empirical artifact correction for proton computed tomography, Physica Medica: European Journal of Medical Physics 86, 57–65 (2021).

[34]. Schultze B, Karbasi P, Sarosiek C, Coutrakon G, Ordoñez CE, Karonis NT, Duffin KL, Bashkirov VA, Johnson RP, Schubert KE, and Schulte RW, Particle-Tracking Proton Computed Tomography—Data Acquisition, Preprocessing, and Preconditioning, IEEE Access 9, 25946–25958 (2021). [PubMed: 33996341]

[35]. Penfold SN, Schulte RW, Censor Y, and Rosenfeld AB, Total variation superiorization schemes in proton computed tomography image reconstruction, Medical Physics 37, 5887–5895 (2010). [PubMed: 21158301]

[36]. Collins-Fekete C-A, Doolan P, Dias MF, Beaulieu L, and Seco J, Developing a phenomenological model of the proton trajectory within a heterogeneous medium required for proton imaging, Physics in Medicine and Biology 60, 5071–5082 (2015). [PubMed: 26061775]

[37]. Collins-Fekete C-A, Volz L, Portillo SKN, Beaulieu L, and Seco J, A theoretical framework to predict the most likely ion path in particle imaging, Physics in Medicine and Biology 62, 1777 (2017). [PubMed: 28076336]

[38]. Giacometti V, Bashkirov VA, Piersimoni P, Guatelli S, Plautz TE, Sadrozinski HF-W, Johnson RP, Zatserklyaniy A, Tessonnier T, Parodi K, Rosenfeld AB, and Schulte RW, Software platform for simulation of a prototype proton CT scanner, Medical Physics 44, 1002–1016 (2017). [PubMed: 28094862]

[39]. Plautz TE, Bashkirov V, Giacometti V, Hurley RF, Johnson RP, Piersimoni P, Sadrozinski HF-W, Schulte RW, and Zatserklyaniy A, An evaluation of spatial resolution of a prototype proton CT scanner, Medical Physics 43, 6291–6300 (2016). [PubMed: 27908179]

[40]. Seco J, Oumano M, Depauw N, Dias MF, Teixeira RP, and Spadea MF, Characterizing the modulation transfer function (MTF) of proton/carbon radiography using Monte Carlo simulations, Medical Physics 40, 091717 (2013). [PubMed: 24007150]

[41]. GAFCHROMIC™ DOSIMETRY MEDIA, TYPE EBT-XD, Accessed: Feb. 24, 2020.

[42]. Martišíková M and Jäkel O, Dosimetric properties of Gafchromic® EBT films in monoenergetic medical ion beams, Physics in Medicine and Biology 55, 3741–3751 (2010). [PubMed: 20530848]

[43]. Fedorov A, Beichel R, Kalpathy-Cramer J, Finet J, Fillion-Robin J-C, Pujol S, Bauer C, Jennings D, Fennessy F, Sonka M, Buatti J, Aylward S, Miller JV, Pieper S, and Kikinis R, 3D Slicer as an image computing platform for the Quantitative Imaging Network, Magnetic Resonance Imaging 30, 1323–1341 (2012), Quantitative Imaging in Cancer.

[44]. Agostinelli S et al. , Geant4—a simulation toolkit, Nuclear Instruments and Methods in Physics Research Section A: Accelerators, Spectrometers, Detectors and Associated Equipment 506, 250–303 (2003).

[45]. Berger MJ, Coursey JS, Zucker MA, and Chang J, ESTAR, PSTAR and ASTAR: Computer Programs for Calculating Stopping–Power and Range Tables for Electrons, Protons and Helium Ions, National Institue of Standards and Technology, 2005.

[46]. Bär E, Andreo P, Lalonde A, Royle G, and Bouchard H, Optimized I-values for use with the Bragg additivity rule and their impact on proton stopping power and range uncertainty, Physics in Medicine & Biology 63, 165007 (2018). [PubMed: 29999493]

[47]. Volz L, Kelleter L, Brons S, Burigo L, Graeff C, Niebuhr NI, Radogna R, Scheloske S, Schömers C, Jolly S, and et al. , Experimental exploration of a mixed helium/carbon beam for online treatment monitoring in carbon ion beam therapy, Physics in Medicine & Biology 65, 055002 (2020). [PubMed: 31962302]

[48]. Kelleter L, Radogna R, Volz L, Attree D, Basharina-Freshville A, Seco J, Saakyan R, and Jolly S, A scintillator-based range telescope for particle therapy, Physics in Medicine & Biology (2020).

[49]. Giacometti V, Guatelli S, Bazalova-Carter M, Rosenfeld AB, and Schulte RW, Development of a high resolution voxelised head phantom for medical physics applications, Phys Med 33, 182–188 (2017). [PubMed: 28108101]

[50]. Hansen DC, Sørensen TS, and Rit S, Fast reconstruction of low dose proton CT by sinogram interpolation, Physics in Medicine and Biology 61, 5868–5882 (2016). [PubMed: 27444677]

[51]. Krah N, Khellaf F, Létang JM, Rit S, and Rinaldi I, A comprehensive theoretical comparison of proton imaging set-ups in terms of spatial resolution, Physics in Medicine & Biology 63, 135013 (2018). [PubMed: 29864022]

[52]. Piersimoni P, Ramos-Méndez J, Geoghegan T, Bashkirov VA, Schulte RW, and Faddegon BA, The effect of beam purity and scanner complexity on proton CT accuracy, Medical Physics 44, 284–298 (2017). [PubMed: 28066887]

[53]. Volz L, Piersimoni P, Johnson RP, Bashkirov VA, Schulte RW, and Seco J, Improving single-event proton CT by removing nuclear interaction events within the energy/range detector, Physics in Medicine & Biology 64, 15NT01 (2019).

[54]. Krämer M, Scifoni E, Schuy C, Rovituso M, Tinganelli W, Maier A, Kaderka R, Kraft-Weyrather W, Brons S, Tessonnier T, Parodi K, and Durante M, Helium ions for radiotherapy? Physical and biological verifications of a novel treatment modality, Medical Physics 43, 1995–2004 (2016). [PubMed: 27036594]

[55]. Mairani A, Dokic I, Magro G, Tessonnier T, Kamp F, Carlson DJ, Ciocca M, Cerutti F, Sala PR, Ferrari A, Böhlen TT, Jäkel O, Parodi K, Debus J, Abdollahi A, and Haberer T, Biologically optimized helium ion plans: calculation approach and its in vitro validation, Physics in Medicine & Biology 61, 4283 (2016). [PubMed: 27203864]

[56]. Besuglow J, Mein S, Kopp B, Tessonnier T, Brons S, Ackermann B, Naumann J, Abdollahi A, Harberer T, Debus J, and Mairani A, WE-B-TRACK 3–1: Towards a Helium Ion-Beam Therapy Program in 2020: Physical, Biological and Clinical Considerations, (2020), Presented at the Joint AAPM | COMP Meeting 2020.

[57]. Welsh JS, DeJongh F, Rykalin V, Karonis N, DeJongh E, Coutrakon G, Ordonez C, Winans J, and Pankuch M, Image Reconstruction with a Fast, Monolithic Proton Radiography System, International Journal of Radiation Oncology * Biology * Physics 99, E737–E738 (2017).

[58]. Esposito M, Waltham C, Taylor JT, Manger S, Phoenix B, Price T, Poludniowski G, Green S, Evans PM, Allport PP, Manolopulos S, Nieto-Camero J, Symons J, and Allinson NM, PRaVDA: The first solid-state system for proton computed tomography, Physica Medica 55, 149–154 (2018). [PubMed: 30420271]

[59]. Pettersen HES et al. , Design optimization of a pixel-based range telescope for proton computed tomography, Physica Medica 63, 87–97 (2019). [PubMed: 31221414]

[60]. Sheng Y, Sun J, Wang W, Stuart B, Kong L, Gao J, You D, and Wu X, Performance of a 6D Treatment Chair for Patient Positioning in an Upright Posture for Fixed Ion Beam Lines, Frontiers in Oncology 10, 122 (2020). [PubMed: 32117769]

[61]. Li X, Liu G, Janssens G, De Wilde O, Bossier V, Lerot X, Pouppez A, Yan D, Stevens C, Kabolizadeh P, and Ding X, The first prototype of spot-scanning proton arc treatment delivery, Radiotherapy and Oncology 137, 130–136 (2019). [PubMed: 31100606]

[62]. Collins-Fekete C-A, Brousmiche S, Hansen DC, Beaulieu L, and Seco J, Pre-treatment patient-specific stopping power by combining list-mode proton radiography and x-ray CT, Physics in Medicine and Biology 62, 6836 (2017). [PubMed: 28657550]

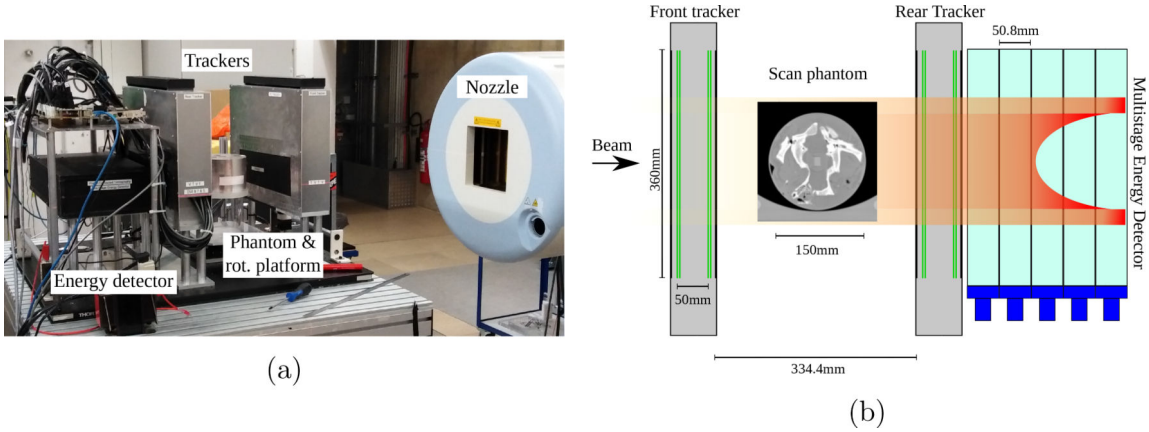

Figure 1:

a) Photograph of the experimental particle CT setup at the HIT experimental cave. b) Schematic depiction of the scanner and phantom together with a sketch of the energy loss distribution in the 5-stage scintillator (view from top).

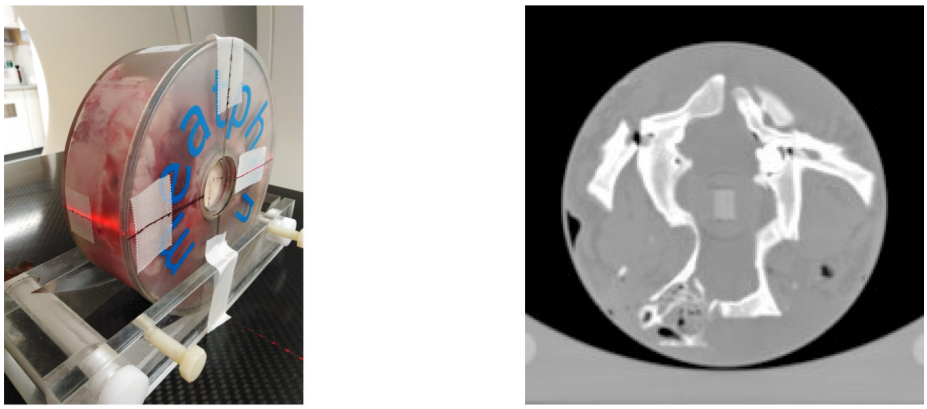

(a) (b)

Figure 2:
Custom designed pig head phantom. Figure (a) Shows the finished phantom, including the brain insert with EBT-XD films. (b) Presents a SECT HU reconstruction of the phantom (C=0HU, W=2000HU).

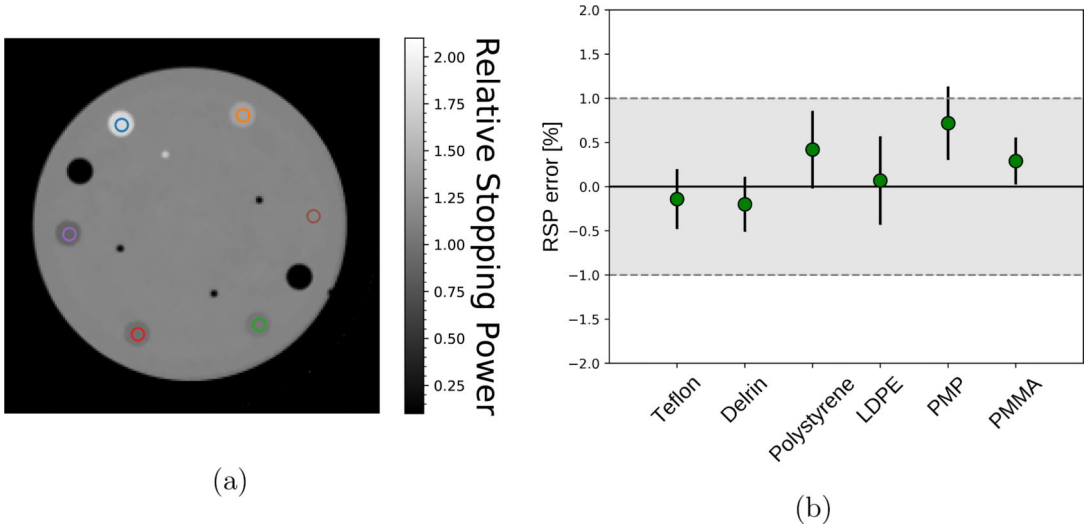

(a) (b)

Figure 3:

a) Reconstructed central slice of an experimental HeCT of the sensitometry module. The colored circles indicate the ROI used for RSP analysis. Blue is Teflon, orange Delrin, brown PMMA, green polystyrene, red LDPE, purple PMP. b) RSP accuracy for the six inserts of the CTP404 sensitometry module as compared to reference measurements. The error bars indicate the standard deviation.

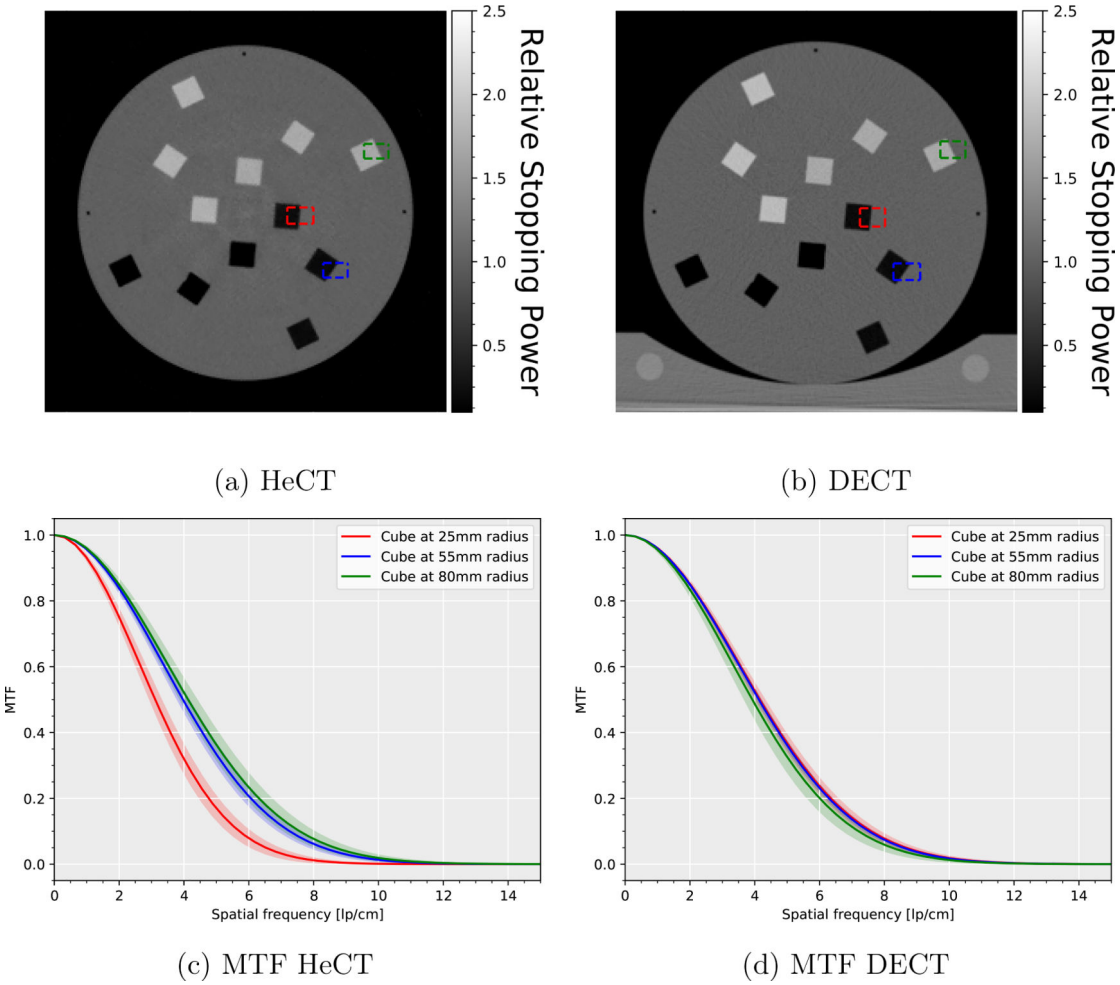

Figure 4:

a) Central slice of an experimental HeCT reconstructed image of the custom spatial resolution phantom. b) Same slice of an RSP converted DECT scan. c) and d) Mean MTFs evaluated from all four cubes at each radial position. The shaded regions indicate the standard deviation. The regions of interest for each cube are shown in a) and b), respectively. The other cubes were assessed by 90° rotations of the image data.

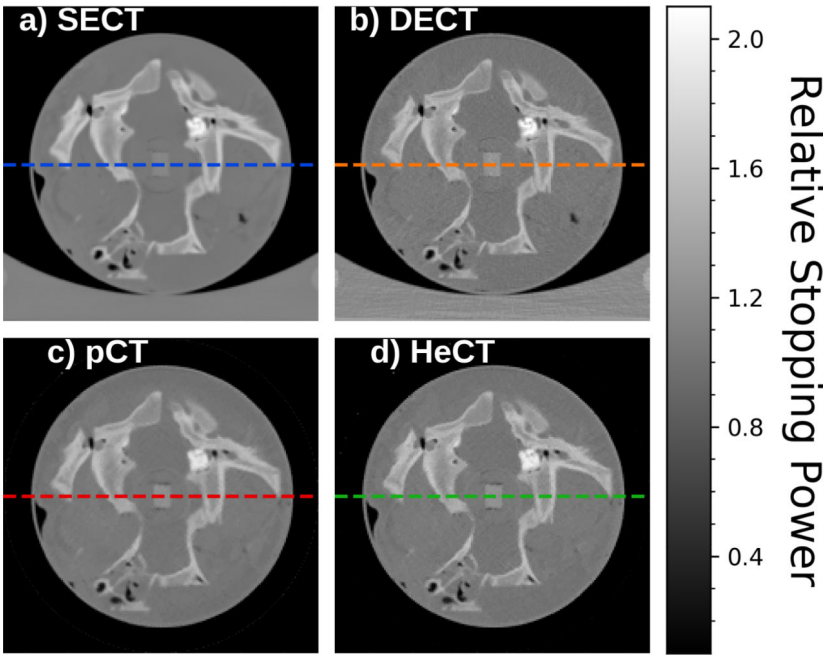

Figure 5:

Slice through the reconstructed CT scans from a) SECT, b) DECT, c) pCT and d) HeCT. Note, the HeCT was reconstructed from 360 projections separated by 1° steps and the pCT from 180 projections separated by 2° steps

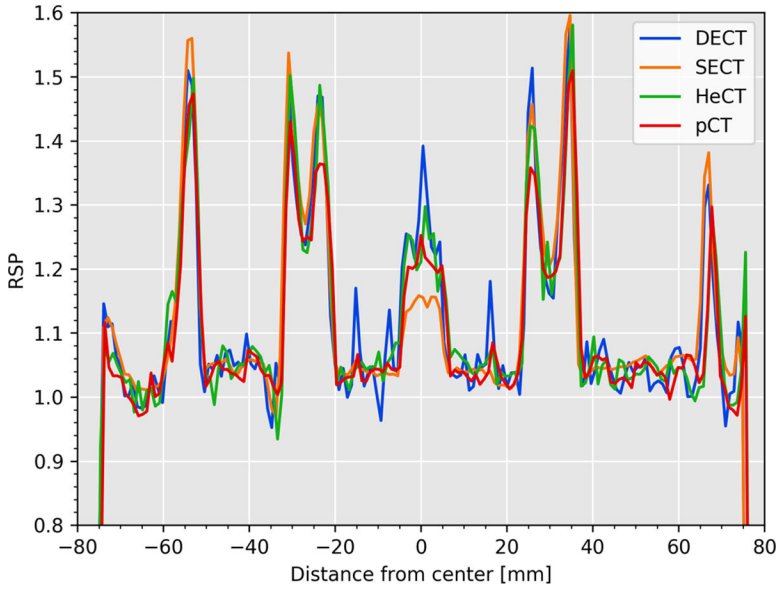

Figure 6:
Line profile through the reconstructed slices of the tissue sample phantom as indicated by the dashed lines in Figure 5.

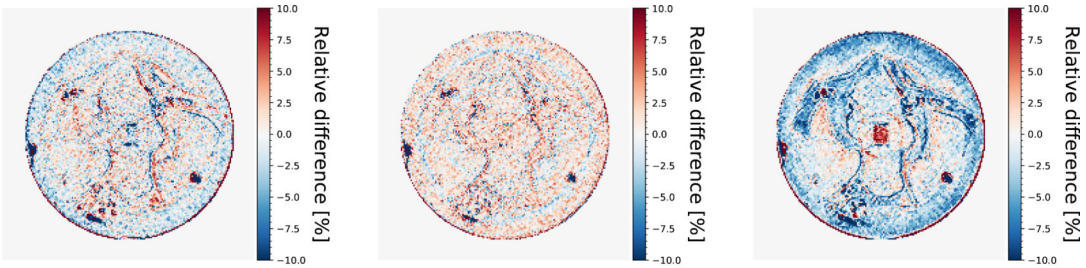

(a) HeCT - DECT (b) HeCT - pCT (c) HeCT - SECT

Figure 7:

Relative difference in RSP between HeCT and the three other modalities investigated for a central reconstructed slice of the custom pig-head phantom after rigid image registration. a) HeCT and DECT, b) HeCT and pCT, c) HeCT and SECT.

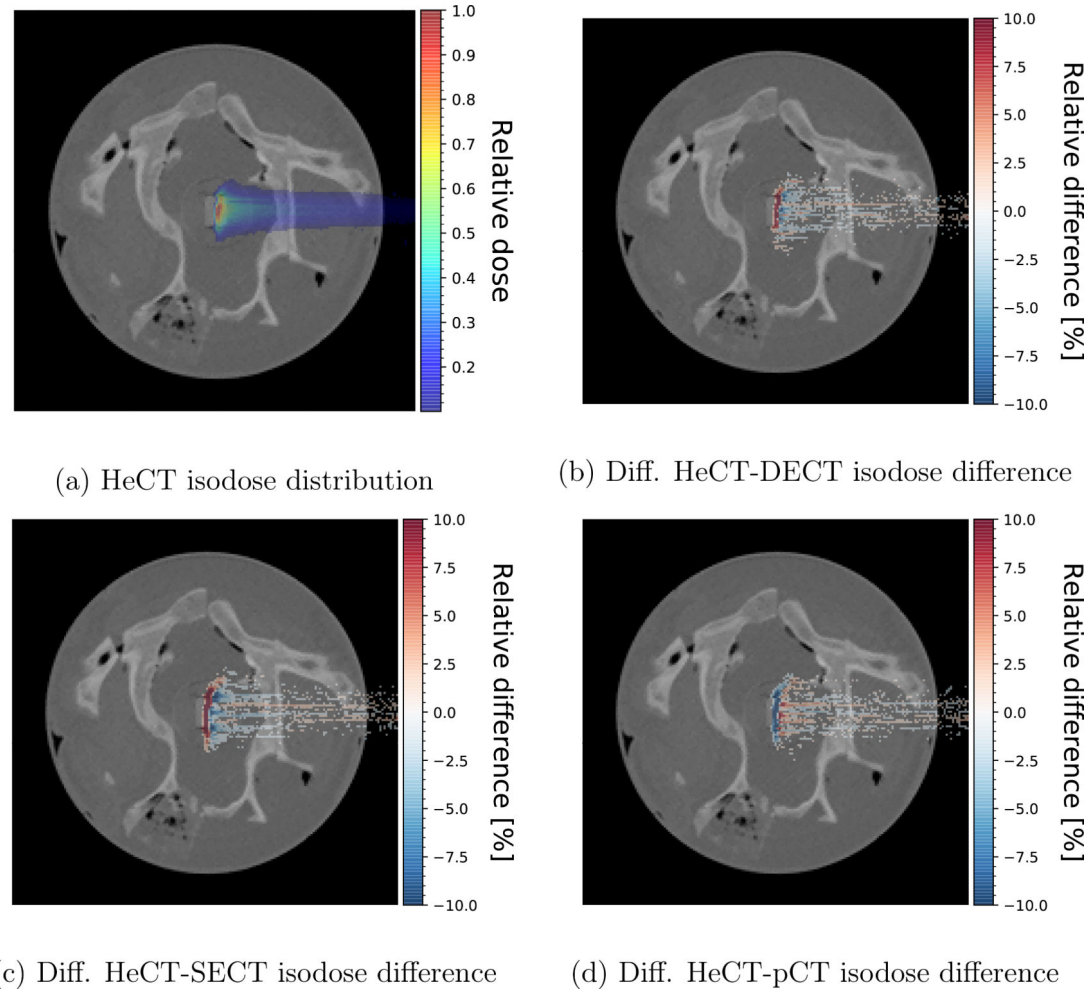

(a) HeCT isodose distribution

(b) Diff. HeCT-DECT isodose difference

(c) Diff. HeCT-SECT isodose difference

(d) Diff. HeCT-pCT isodose difference

Figure 8:

a) Dose distribution of the proton beam as simulated in a Geant4 Monte Carlo simulation based on the HeCT reconstruction of the pig-head phantom. The dose was normalized to the maximum value. b)-d) Relative difference between the dose calculated on HeCT and that of DECT, SECT and pCT, respectively, in percent of the peak dose of the proton beam. Values below 1% of the peak dose where masked. The difference maps are overlayed on the HeCT reconstructed slice.

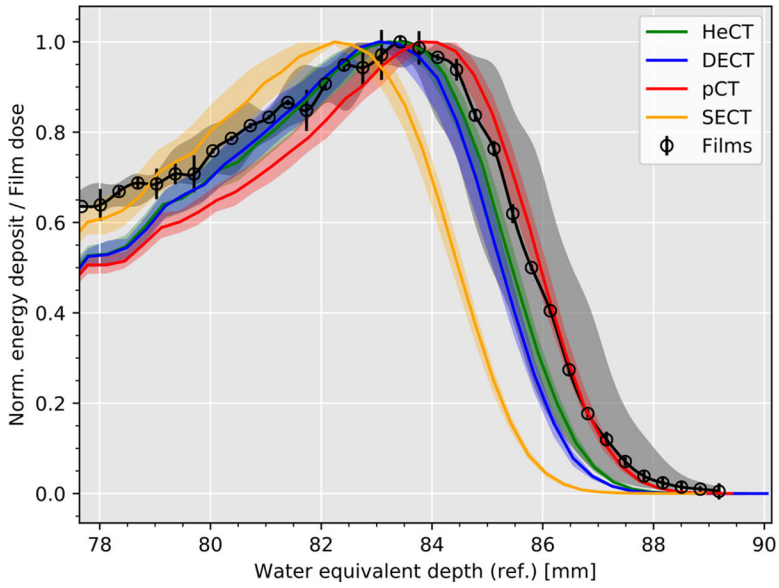

Figure 9:

Comparison between the film measured proton depth dose curve, and the Monte Carlo simulated depth dose curves based on each CT modality. Shaded regions correspond to the uncertainty, the error bars of the film reference indicate the difference between the two measurements performed to generate the curve.